Tellus (1984), *36A*, 172–186

Numerical studies of stratified air flow over a mountain ridge on the rotating earth

By ARNT ELIASSEN and SIGURDUR THORSTEINSSON, *Institute of Geophysics, University of Oslo, P.O. Box 1022, Blindern, Oslo 3, Norway*

(*Manuscript received February 7; in final form May 17, 1983*)

ABSTRACT

The non-linear equations describing adiabatic, quasi-static flow of stably stratified air over a mountain ridge on the rotating *f*-plane are integrated numerically in time, using potential temperature as vertical coordinate. The initial state is a horizontal, parallel flow over level ground, and the cosine-shaped, 400 km wide ridge, oriented normal to the initial flow, is allowed to grow to full height in 20 h. The potential vorticity remains constant in each isentropic surface, and this condition is used in the calculations instead of the mass continuity equation.

Results of calculations starting with 4 different initial wind profiles are shown. After about 5 model days of integration, the motion within the integration area of length 4 Mm settled down to a nearly steady flow. This flow exhibits a system of gravity-inertia lee waves with dominating wavelengths comparable to the mountain width. The prominent wavelengths seem in all calculations to be limited to waves shorter than the inertia wavelength at the lower boundary (for which the particle frequency equals the Coriolis parameter). The waves are discussed in the light of linear theory and ray tracing. In a case where the initial wind velocity decreases with height, there is a clear tendency towards formation of pure horizontal, undamped inertia waves in the layer of wind shear, with cycloid-shaped horizontal trajectories.

Besides the wave pattern, the stationary flow also shows a large-scale turning of the streamlines, to the left on the upstream side and to the right on the lee side, with a distinct anticyclonic bend over the mountain ridge. The formation of this turning is explained as a consequence of the loss of mass through the open boundaries connected with the growth of the mountain; thus the turning depends on the formulation of the inflow and outflow boundary conditions. Unless the large-scale turning is strictly symmetric with respect to the mountain ridge, the flow will possess a component along the ridge, with a corresponding geostrophic pressure gradient which together with the wave drag will contribute to the total horizontal force acting on the mountain.

1. Introduction

The character of air flow over hills and mountains depends primarily on the horizontal scale of the orographic features, or more precisely on the Rossby number defined by means of the typical mountain half-width and the current velocity. For flow over small-scale orographic features at large Rossby numbers (of order ten or more), the earth's rotation has little effect, and the theory of the resulting gravity wave pattern can be simplified by ignoring the rotation altogether. At the opposite end of the spectrum, flow over extensive mountain areas at small Rossby numbers, simplification is achieved by utilizing the quasi-geostrophic character of the flow. In the middle part of the spectrum, here termed meso-scale, the Rossby number is of the order one. At normal wind velocities, this would correspond to mountains with half-width of the order of a hundred or a few hundred kilometres, as e.g. the Alps, Iceland, Scandinavia. The flow over these mountains is strongly affected by the earth's rotation, but is not quasi-geostrophic. Therefore, neither of the simplifications mentioned above are applicable. This is perhaps the reason for the scarcity of theoretical studies of this type of flow.

Also from an observational point of view, flow over meso-scale mountains is difficult to study. Small-scale gravity lee waves can be mapped by air planes, and are well-known due to the familiar lenticular clouds which often make the wave motion visible. Large-scale oreigenic flow which is quasi-geostrophic, can be studied from maps of the geostrophic flow field. However, meso-scale mountain waves are too small to be mapped by the normal network of radiosonde stations, and the corresponding wave clouds are too large to be identified as such by an observer on the ground. Such wave clouds are probably also very much disturbed by horizontal humidity gradients in the air flow.

The linearized equations describing flow of stratified air with rotation over a mountain ridge of small height was first studied by Queney (1947, 1948). In these classical papers, he gave the stationary solution in the form of a Fourier integral, and was able to evaluate the integral, using the method of stationary phase, in the case of barotropic basic flow with constant buoyancy frequency.

The more realistic case, with the basic velocity possessing vertical shear, was studied by Jones (1967). In this case, the Fourier integral has a singularity at the particular horizontal wave number for which the particle frequency equals the Coriolis parameter; this wave number varies with height in inverse proportion to the velocity of the basic flow. Eliassen (1968) demonstrated that the mathematical singularity corresponds to the formation of an undamped train of pure inertia waves on the lee side. One of the objectives of the present work was to study numerically the formation of such inertia waves.

Numerical calculations of the air flow over a meso-scale mountain ridge from the non-linear equations were made by Eliassen and Rekustad (1971), hereafter referred to as ER. With realistic wind and temperature profiles, they found meso-scale mountain waves of considerable amplitude throughout the troposphere over the mountain and on its lee side; but they did not find the undamped inertia wave mentioned above. However, such waves do show up in some of the calculations shown in the present paper. These calculations were made with a very similar model, but with more detail and better accuracy than in ER. Following a suggestion of Ronald Smith (personal communication), we have made the computations for different idealized vertical wind profiles, but with the same constant value of the static stability parameter N. This is consistent with the result from linear theory that while a change with height of N just gives a corresponding mild change of the vertical wavelength, a vertical wind shear implies a change with height of the singular wave number and may have a more profound effect on the wave field.

2. Mathematical formulation

The notation used in the following is given in the Appendix.

We consider adiabatic flow of stable stratified air over a straight mountain ridge on the rotating f-plane. We are primarily interested in the characteristics of stationary flow. However, for the purpose of numerical calculation we follow the approach in ER and consider the initial value problem where the initial state is a straight horizontal flow over level ground; the ground topography is then allowed to grow to its final height in a finite time, and the resulting transient flow is calculated until it settles to a nearly steady state.

Following ER, we use θ as vertical coordinate and assume that the motion is two-dimensional in the sense that the velocity components u, v are independent of y at all times. A necessary requirement then is that the horizontal pressure gradient force $(-m_x, -m_y)$ is also independent of y. In a situation where the cross stream gradient is independent of time, U must at all times represent the x-component of the geostrophic wind:

$$U_x = U_y = 0, \qquad U = -f^{-1} m_y = U(\theta), \tag{2.1}$$

with subscripts denoting differentiation. (Notice that partial derivatives with respect to x, y, t are taken at constant θ.)

Since U is allowed to vary with height, p must vary with y in accordance with the thermal wind equation

$$p_y = -fU_\theta/\Pi'(p). \tag{2.2}$$

Consequently, the continuity equation will contain a term $vp_{y\theta}$. However, as pointed out in ER, this term has negligible effect upon the meso-scale

mountain waves, and will be omitted in the present paper.

As in ER, we use a Rayleigh friction "sponge" in the upper layers in order to absorb rather than reflect wave energy at the upper boundary. In contrast to ER, however, we apply the Rayleigh friction in the x-momentum equation only. By dropping it in the y-momentum equation, we attain exact conservation of potential vorticity.

With these simplifications, the equations of motion, mass continuity and hydrostatic equilibrium are

$$u_t + uu_x - fv + m_x = -\kappa(u - U), \tag{2.3}$$

$$v_t + uv_x + f(u - U) = 0, \tag{2.4}$$

$$p_{\theta t} + (up_\theta)_x = 0, \tag{2.5}$$

$$m_\theta = \Pi(p). \tag{2.6}$$

From (2.4) and (2.5) we derive

$$q_t + uq_x = 0, \tag{2.7}$$

where

$$q = \frac{f + v_x}{-p_\theta} \tag{2.8}$$

is the potential vorticity. The lack of a y-advection term in (2.7) is a consequence of our omission of such a term in (2.5). This simplifying assumption is thus equivalent to assuming $q_y = 0$ everywhere. As a further consequence, our equations describe a system which is barotropically and baroclinically stable; with θ constant at the upper and lower boundary (see below), this follows from the Charney-Stern (1962) theorem. The upper boundary at $\theta = \theta_T$ is assumed to be a free surface with constant pressure p_T; thus

$$p(x, \theta_T, t) = p_T, \qquad \text{or} \qquad m_\theta(x, \theta_T, t) = \Pi(p_T). \tag{2.9}$$

The ground is assumed to coincide with an isentropic surface $\theta = \theta_G$, and its height is prescribed as follows:

$$z(x, \theta_G, t) = g^{-1}(m - \theta m_\theta)_{(\theta=\theta_G)} = z_G(x)\,\alpha(t)$$

$$= \alpha(t) h h_1\left(\frac{x}{2a}\right). \tag{2.10}$$

Here $h_1(\xi)$ gives the ridge profile, a its half-width, and h the crest-height (assumed to be located at $x = 0$, with $h_1(0) = 1$). The factor $\alpha(t)$ is defined to be zero initially and to grow gently to unity during some finite time interval.

The initial state is taken to be a straight horizontal flow $U(\theta)$ in geostrophic and hydrostatic equilibrium; thus the initial Montgomery potential $M(y, \theta)$ satisfies

$$M_y = -fU, \qquad M_\theta = \Pi(P), \tag{2.11}$$

where $P(y, \theta)$ is the initial pressure distribution. M and P must satisfy the boundary conditions (2.9) and (2.10), with $\alpha(0) = 0$.

To complete the definition of the initial state, we must also define the vertical temperature profile. The hydrostatic equation may be expressed as

$$\Pi(P)_\theta = -g^2 N^{-2} \theta^{-2}. \tag{2.12}$$

We shall assume the buoyancy frequency N to be constant in the vertical plane $y = 0$. Then from (2.12) and (2.2),

$$\Pi(P) = \Pi(p_T) + \frac{g^2}{N^2}\left(\frac{1}{\theta} - \frac{1}{\theta_T}\right) - fU_\theta y, \tag{2.13}$$

and from (2.11)

$$M(y, \theta) = \Pi(p_T)\theta + \frac{g^2}{N^2}\left(\frac{\theta_T - \theta}{\theta_T} + \ln\frac{\theta}{\theta_G}\right) - fUy \tag{2.14}$$

These equations, applied at $y = 0$, complete the definition of the initial state.

Since the initial velocity is uniform in each isentropic surface, the potential vorticity is initially equal to $Q = f/(-P_\theta)$. Eq. (2.7) may then be integrated to

$$q(x, \theta, t) = Q(\theta) \qquad \text{or} \qquad \frac{f + v_x}{-p_\theta} = \frac{f}{-P_\theta}, \tag{2.15}$$

expressing that q is constant in each isentropic surface.

Consider a hypothetical air particle moving with the geostrophic wind. Its horizontal trajectory $y = y_0 + \eta_g(x)$ must satisfy

$$\frac{d\eta_g}{dx} = -\frac{m_x}{m_y} = (fU)^{-1} m_x. \tag{2.16}$$

On the other hand, a real air trajectory $y = y_0 + \eta(x)$ satisfies

$$\frac{d\eta}{dx} = \frac{v}{u}. \tag{2.17}$$

If the motion is stationary, the trajectory coincides with the streamline and may be obtained from the Bernoulli equation:

$$\frac{d\eta}{dx} = (fu)^{-1}\,[m + \tfrac{1}{2}(u^2 + v^2)]_x. \tag{2.18}$$

The vertical profile of an isentropic surface in the xz-plane may be obtained from

$$gz(x, \theta) = m - \theta m_\theta. \tag{2.19}$$

This is not quite the same as the vertical projection $\zeta(x)$ of a three-dimensional particle trajectory, because the particle also moves sideways along the sloping isentropic surface. We have

$$\zeta(x) = z(x, \theta) - \eta(x)\ (U - \theta U_\theta) f/g. \tag{2.20}$$

The last term represents the displacement motion of the particle due to the lateral slope of the isentropic surfaces. In a barotropic current the isentropic surfaces have just the small isobaric slope, and z does not significantly differ from ζ; but the difference may be noticeable in strongly baroclinic flow.

3. The numerical model

It is noteworthy that finite difference analogues to the four equations (2.3–2.6) do not necessarily yield an analogue of (2.7), expressing conservation of a finite difference approximation to potential vorticity. In particular, the numerical scheme employed in ER (without the friction term) does not yield a rigorous potential vorticity conservation equation. Indeed, preliminary integrations with that model showed that significant changes of finite difference approximations to the potential vorticity may occur within the inviscid part of the fluid; these changes are just truncation errors.

Following a suggestion by Hans Økland (personal communication), we shall here replace the mass continuity equation (2.5) by the integrated potential vorticity equation (2.15). Of course, this can be done only when the potential vorticity equation can be integrated, i.e. when the potential vorticity is constant in isentropic surfaces.

Apart from this change, our finite difference scheme (centred differences, leapfrog) is the same as in ER; it is based on a rectangular grid ($i\Delta x$, $\theta_G + j\Delta\theta$, $n\Delta t$) in the $x\theta$-plane. Thus our finite difference equations are

$$\delta_t u = fv - \delta_x(m + \tfrac{1}{2}u^2) - \kappa(u^* - u), \tag{3.1}$$

$$\delta_t v = -u\delta_x v - f(u - u), \tag{3.2}$$

$$\delta_\theta p = (1 + f^{-1}\delta_x \bar{v}^\theta)\delta_\theta P, \tag{3.3}$$

$$\delta_\theta m = \overline{\Pi(p)}^\theta, \tag{3.4}$$

consisting of two prognostic and two diagnostic equations.

The symbols δ and $\bar{\ }$ are the centred difference and average operations over one grid mesh. At time instants $n\Delta t$, u, m, and p are given in points (i,j) and v in $(i + \frac{1}{2}, j)$; and vice versa at time instants $(n + \frac{1}{2})\,\Delta t$. Thus the grid is staggered in x and t, but not in θ. u^* in the friction term is taken at the previous time step.

When u and v are known up to time t, $p(t)$ is obtained from (3.3) by vertical integration, starting from the top where p is known from (2.9). Then $m(t)$ is obtained from (3.4) by vertical integration starting from the bottom where, according to (2.10), m has the value

$$m_G = \theta_G\,\Pi(p_G) + \alpha(t) g h h_1\left(\frac{x}{2a}\right). \tag{3.5}$$

Finally, $u(t + \frac{1}{2}\Delta t)$ and $v(t + \frac{1}{2}\Delta t)$ are calculated from (3.1) and (3.2), and the procedure is repeated.

From (3.2) and (3.3) we derive for later reference the equation of mass continuity in the form which is consistent with our numerical model:

$$\delta_t(-\delta_\theta p) = -\delta_x F_M. \tag{3.6}$$

Here F_M is a measure of the horizontal mass flux through a thin isentropic layer:

$$F_M = \frac{\overline{(f + \delta_x v)u}^\theta}{f + \delta_x \bar{v}^\theta}(-\delta_\theta p) = \overline{(f + \delta_x v)u}^\theta \frac{(-\delta_\theta P)}{f}. \tag{3.7}$$

We may assume the analytically formulated model of Section 2 to be of infinite extent in the x-direction. Since the characteristic velocities are finite, the analytical model is thus physically closed; the present state of the model uniquely determines the future states. By contrast, the numerical model must be delimited to a finite interval (x_A, x_B). This model is thus of finite extent and possesses two open boundaries $x = x_A$, x_B through which exchange of mass, momentum and

energy with the environment takes place. Therefore, the instantaneous state of the numerical model does not alone determine its future states, since these may also be influenced by processes in the environment.

Mathematically, the influence of the environment must be formulated as boundary conditions for the open boundaries. Clearly, if the environment is disturbed in an unknown manner, such a formulation is not possible, and a time integration cannot be performed. The numerical integrations are based on the assumptions that the environment is initially at rest and does not contain any sources of mass, momentum or energy within finite distances; all processes in the environment are caused by the disturbances inside the model. Thus the boundary conditions should allow wave energy inside the system to leave through the boundaries, rather than being reflected.

Here we have adopted the extrapolation scheme described by Orlanski (1976), with a modification introduced by Klemp and Lilly (1978). This method is used to obtain the boundary values of both u and v, at the inflow boundary as well as the outflow boundary. Referring to Fig. 1, which represents a few grid-points with u-values in the xt-plane at and next to the outflow boundary, the method may be briefly described as follows. First, a local propagation velocity c is determined from

$$c = \begin{cases} 0 & \text{if} \quad \beta \le 0 \\ \beta \dfrac{\Delta x}{\Delta t} & \text{if} \quad 0 < \beta < 1 \\ \dfrac{\Delta x}{\Delta t} & \text{if} \quad \beta \ge 1, \end{cases}$$

$$\beta = \frac{u_1 - u_4}{u_2 - u_3}. \tag{3.8}$$

Then u_5 is obtained from

$$u_5 = \left(1 - \frac{2}{1 + \dfrac{\Delta x}{c\,\Delta t}}\right) u_2 + \frac{2}{1 + \dfrac{\Delta x}{c\,\Delta t}}\, u_4. \tag{3.9}$$

Before applying (3.9), the c-values were smoothed by means of a three-point Shapiro (1970) filter, involving the adjacent points above and below.

The same procedure was used to obtain the boundary values of v. At the inflow boundary, corresponding formulas with opposite symmetry were used. To remove spurious two gridpoint-waves formed by the inflow and outflow boundary conditions, the five-point spatial filter designed by Shapiro (1970) was applied to the fields of u and v every $100\Delta t$ unless otherwise indicated. For the purpose of filtering values at or next to the open boundaries, the grid was extended by two points outside the boundary, with values of u and v equal to those in the boundary gridpoint.

To obtain the boundary values of p, we have not used the Orlanski-type condition, but instead applied the potential vorticity eq. (3.3), with $\delta_x v$ replaced by a one-sided difference centred in time.

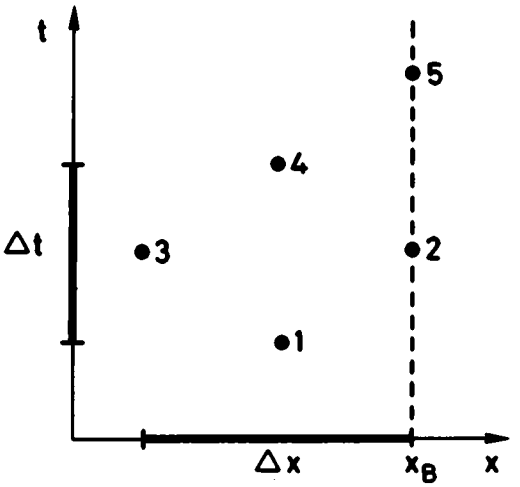

Fig. 1. Configuration of points near outflow boundary, referred to in eqs. (3.8) and (3.9).

4. Numerical calculations

The result of five integration experiments (Experiments 1–5) performed with the described model are presented below. In all these experiments, the mountain profile was

$$h_1\left(\frac{x}{2a}\right) = \begin{cases} \dfrac{1}{2}\left(1 + \cos\dfrac{\pi x}{2a}\right), & |x| < 2a \\ 0, & |x| \ge 2a. \end{cases} \tag{4.1}$$

The mountain grew from zero to full size in 20 h. The $x\theta$-grid consisted of the points $i = 0, 1, \ldots, 80$ in the x-direction and 51 θ-surfaces $j = 0, 1, \ldots, 50$. The Rayleigh friction coefficient was taken to be a function of j:

$$\kappa_j = \begin{cases} \kappa_T \sin^2 \dfrac{\pi}{2} \dfrac{\ln(\theta_j/\theta_{30})}{\ln(\theta_T/\theta_{30})}, & j > 30 \\ 0, & j \le 30. \end{cases} \qquad (4.2)$$

The following numerical values were used:

$\theta_G = 275$ K, $p_G = 1$ bar $= 10^5$ Pa,

$\Delta x = 50$ km, $x_A = -1750$ km,
$x_B = 2250$ km,

$\Delta t = 110$ s, $f = 1.3 \times 10^{-4}$ s^{-1},
$N = 1.3 \times 10^{-2}$ s^{-1},

$a = 100$ km, $\kappa_T = 1.34 \times 10^{-4}$ s^{-1}.

In Experiments 1–4, the integration was carried to 122 h (4000 Δt) and in Experiment 5 to 137.5 h (4500 Δt). At these times, the wave fields were very nearly stationary throughout the region of integration.

The results of the numerical integration (Experiments 1–5) are shown in Figs. 2–6, each of which has two parts, labelled a and b. The a-figures represent the xz plane and its intersection curves with the isentropic surfaces $j = 0, 2, 4, \ldots, 30$, obtained from expression (2.19) for z. We do not show the vertical streamline displacement ζ, since its deviation from z was quite small in the cases studied. The b-figures show, for the same isentropic surfaces, the horizontal projection of a geostrophic streamline η_g (dashed curves) and a real streamline η (solid curves). They were calculated from (2.16) and a trapezoidal integration of (2.17), respectively. An alternative calculation of η from (2.18) gave very nearly the same result, indicating that the flow was stationary to a good approximation.

The initial velocity profile, drawn to the scale of $L_f = 2\pi U/f$, is shown on both a- and b-figures.

The five experiments (1–5) differed from each other in having different initial velocity profiles, different mountain heights, and different choice of isentropic grid surfaces, as summarized in Table 1. Four types of velocity profile were used: no vertical shear, positive shear, negative shear, and both positive and negative shear. Except for Experiment 1, the mountain height was taken nearly as high as possible without causing the calculation to break down.

The vertical grid resolution ($\Delta\theta$) was to a certain extent adjusted to fit the vertical scale of the wave field.

5. Computed wave patterns

It is apparent from Figs. 2–6 that two kinds of perturbation are produced in the air flow: a stationary pattern of gravity-inertia waves above and to the lee of the mountain, with dominating wavelengths comparable with the width of the

Table 1. *Data concerning numerical experiments*

Experiment no.	j	$\Delta\theta$ (K)	j	U_j (m s^{-1})	h (m)	Calculated drag (N m^{-1})
1	0–30	2.6	0–50	13	10	7.3
	30–50	3.0				
2	0–30	2.6	0–50	13	800	$1.61 \cdot 10^5$
	30–50	3.0				
3	0–18	2.1	0–4.5	10		
	18–40	3.3	4.5–16.5	$10 + 0.5\,(j - 4.5)$	800	$1.06 \cdot 10^5$
	40–50	3.7	16.5–50	16		
			0–7.5	16		
4	0–20	2.6	7.5–19.5	$16 - 0.5(j - 7.5)$	700	$1.41 \cdot 10^5$
	20–50	2.1	19.5–50	10		
			0–7.5	$10 + 0.8j$		
5	0–20	2.6	7.5–19.5	$16 - 0.5(j - 7.5)$	800	$1.06 \cdot 10^5$
	20–50	2.1	19.5–50	10		

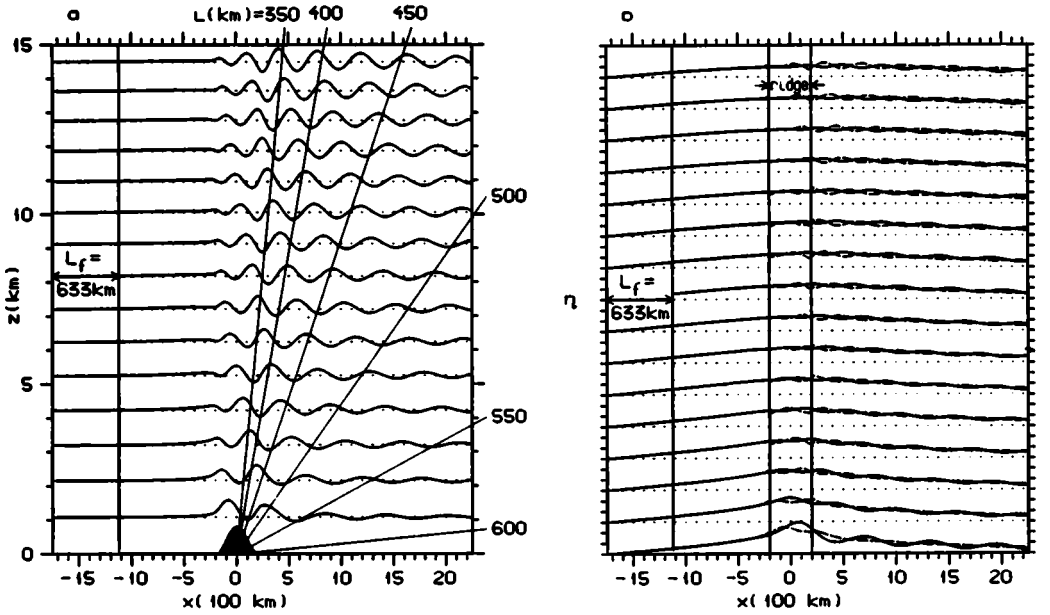

Fig. 2. Experiment 1. (a) xz-plane showing the intersection curves with the isentropic surfaces $j = 0, 2, \ldots, 30$ (heavy lines), and wave rays for selected values of the horizontal wave length L (thinner lines). (b) Horizontal projection of air trajectories $\eta(x)$ (solid curves) and geostrophic trajectories η_g (dashed), for the same isentrophic surfaces, $j = 0, 2, \ldots, 30$. The vertical profile of $L_f = 2\pi U/f$ is shown to the left in both figures. See Table 1 for further details.

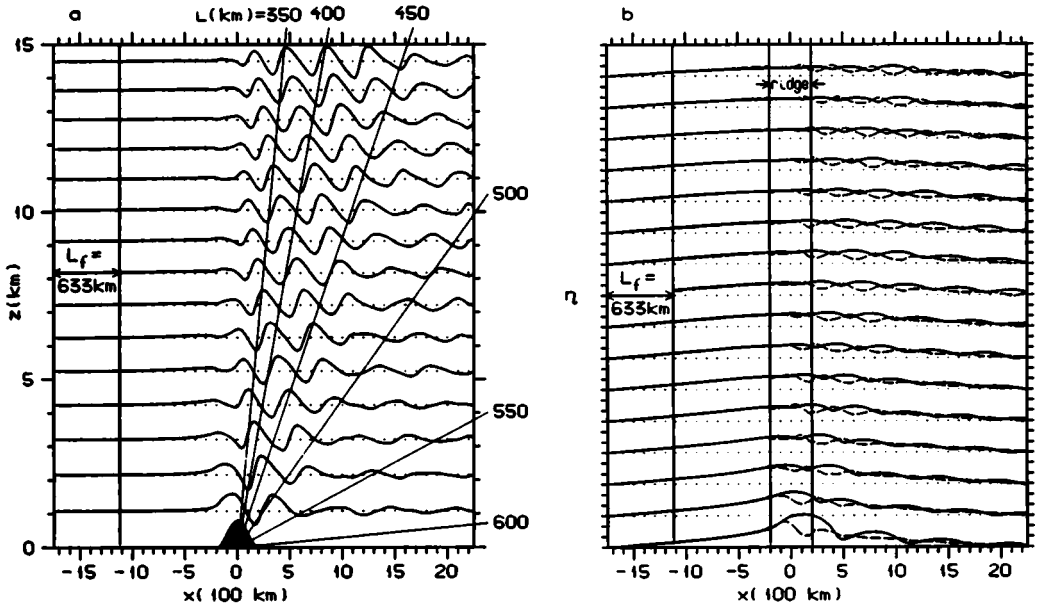

Fig. 3. Experiment 2 (cf. legend for Fig. 2).

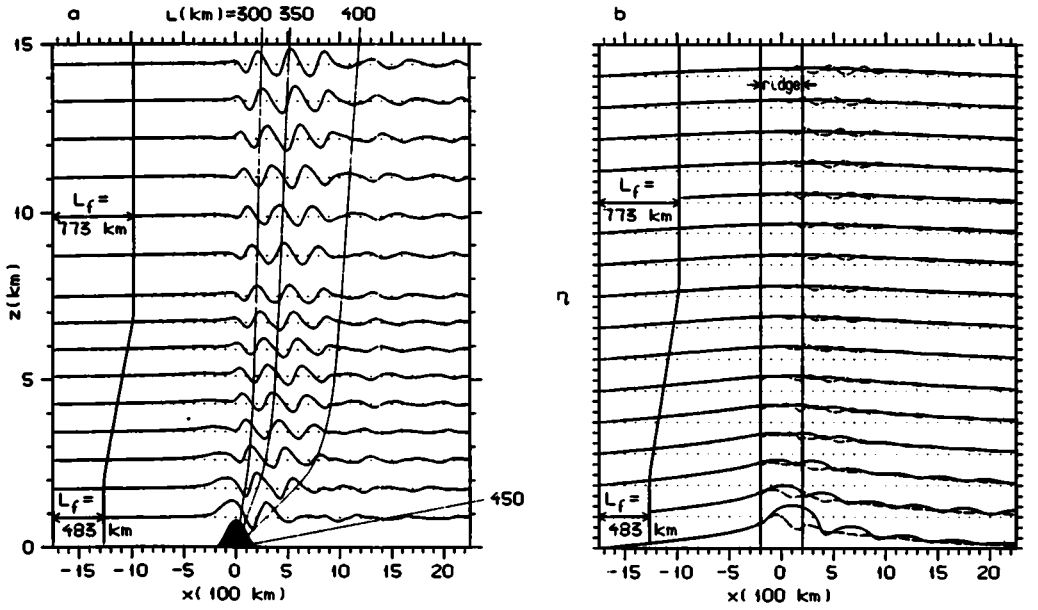

Fig. 4. Experiment 3 (cf. legend for Fig. 2).

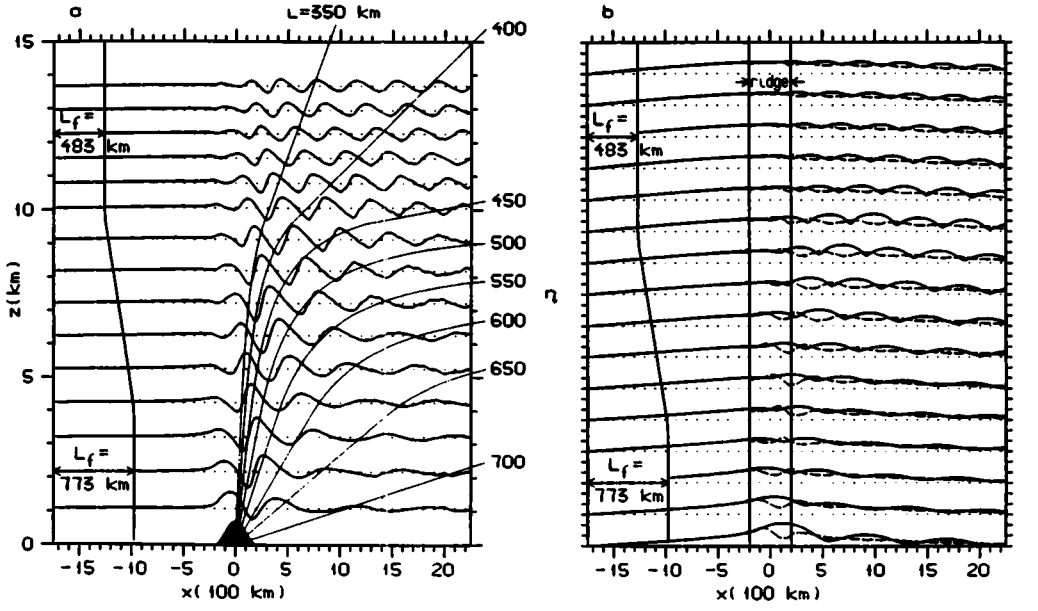

Fig. 5. Experiment 4 (cf. legend for Fig. 2).

mountain; and in addition, a large-scale turning of the air current, to the left on the upstream side, and to the right on the lee side. Discussion of the latter effect will be deferred to Section 6; in the present section we will consider only the gravity-inertia waves.

Experiments 1 (Fig. 2) and 2 (Fig. 3) both refer to an initially constant current (U = 13 m s^{-1} at all

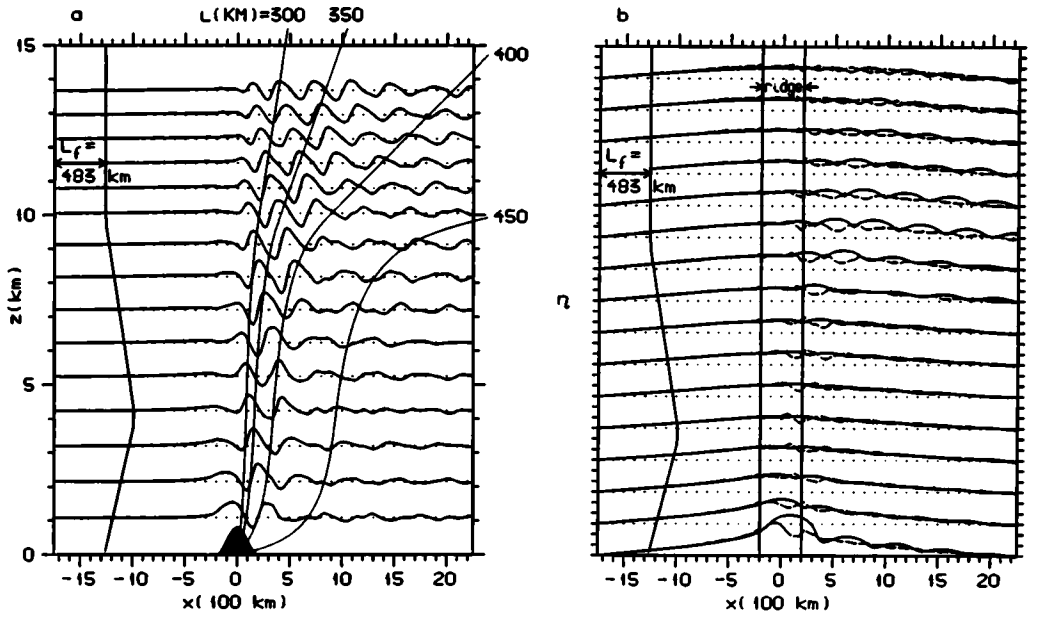

Fig. 6. Experiment 5 (cf. legend for Fig. 2).

levels) and a mountain height 800 m. However, while Experiment 2 represents the full non-linear solution, Experiment 1 was computed for a mountain only 10 m high, and then magnified by a factor 80. Thus, Fig. 2 corresponds very closely to the numerical solution of the linearized equations. The flow field may be described as a pattern of nearly sinusoidal waves, with amplitudes and local wavelengths varying slowly in space. Queney (1947, 1948), in his pioneering theoretical studies, obtained very much the same picture from an analytical solution of the linear equations.

Many properties of the result can be explained from the theory of dispersive waves in a slowly varying medium (Whitham, 1974). According to this theory, the waves behave locally as plane waves which, in the case of stationary motion in a current of constant velocity U may be expressed as

$$\zeta = \text{Real part}\left\{\zeta_0\left(\frac{\rho_0(0)}{\rho_0(z)}\right)^{1/2} \times \exp 2\pi i\left(\frac{x}{L}+\frac{z}{H}\right)\right\}. \tag{5.1}$$

Here ζ is the vertical particle displacement, ζ_0 the amplitude of a corrugated ground, $\rho_0(z)$ the density in the basic state, and L the horizontal and H the vertical wavelength.

With the notation

$$H_N = \frac{2\pi U}{N}, \qquad L_f = \frac{2\pi U}{f}, \tag{5.2}$$

the vertical wavelength H is, to a good approximation given by

$$H = H_N\sqrt{1 - L^2/L_f^2}. \tag{5.3}$$

Thus, H decreases from H_N for short waves towards zero when L approaches L_f. When $L > L_f$, H becomes imaginary, corresponding to exponential change of ζ with height.

Expression (5.1) represents a stationary wave with phase lines tilted upstream with height, in accordance with the upward transfer of wave energy and downward momentum flux. The slope of the phase lines is $-H/L$.

In Fig. 2, with $H_N = 6.3$ km, $L_f = 630$ km, the local values of H and L are in excellent agreement with eq. (5.3). The phase lines also have the required upwind tilt.

As pointed out by Klemp and Lilly (1980), the distribution of local wavelengths in space may be inferred from ray tracing theory. Relative to the resting mountain, the components of the group

velocity are, to a good approximation when $L \gg H_N$,

$$c_{gx} = U(L/L_f)^2, \quad c_{gz} = c_{gx}\frac{f}{N}\left(\left(\frac{L_f}{L}\right)^2 - 1\right)^{3/2}. \tag{5.4}$$

Thus, c_{gx} and c_{gz} are both positive, and the rays

$$\frac{dz}{dx} = \frac{c_{gz}}{c_{gx}} \tag{5.5}$$

slope upward in the downstream direction. The energy of the wave field may be considered to be maintained by radiation of wave energy along rays originating in the mountain, which represents the source of wave energy. In the present case of constant U and N, the medium is homogeneous as far as wave propagation is concerned, and the rays are straight lines. It follows from (5.4) and (5.5) that the steepness of the rays decreases with increasing horizontal wavelength. The energy of waves much shorter than L_f is carried upward along almost vertical rays, while the energy of waves with L approaching L_f is transferred downstream along almost horizontal rays. Rays corresponding to selected values of L are shown as thin lines in Fig. 2. These values are seen to correspond very closely to the local wavelengths in the computed wave field. Waves with $L > L_f$ do not show up, because they are strongly damped out with height.

Finally, we may use the wave-action principle to calculate the change of wave amplitude A along the rays. Since wave energy density is proportional to $\rho_0 A^2$ and the particle frequency is proportional to U, the wave-action equation for stationary flow (Whitham, 1974) becomes

$$\nabla \cdot (c_g \rho_0 A^2/U) = 0$$

or

$$c_g \cdot \nabla \ln (\rho_0 A^2/U) = -\nabla \cdot c_g. \tag{5.7}$$

In the present case, U = constant,

$$c_g = c_g\, r/r, \quad \nabla \cdot c_g = c_g/r$$

and eq. (5.7) gives simply, along every ray,

$$\rho_0 A^2 \sim \frac{1}{r} \tag{5.8}$$

This relation also seems to be well satisfied by the computed wave field in Fig. 2.

Fig. 3 (Exp. 2) shows the non-linear solution with the same mountain height and wind profile as for the linear solution shown in Fig. 2. Comparing the vertical wave patterns in the two figures, three differences stand out: the non-linear waves of Fig. 3a have somewhat larger amplitudes, are steepened on the upwind side, and the whole pattern is displaced 100–150 km downstream relative to the linear wave field. Moreover, while the horizontal undulations of the streamlines in the linear calculation of Fig. 2b have nearly the shape of sine waves, in the non-linear calculation Fig. 3b the waves have sharp cyclonic turns, which are clearly connected with u almost vanishing at these points.

Even with these non-linear effects present, the computed wave field in Fig. 3 is still sufficiently similar to the linearized wave field in Fig. 2 so that its main features can be explained on the basis of conservation of horizontal wavelength and wave action along the rays.

Next we turn to Experiment 3, showing a case where L_f increases from 483 km in the lowest 2 km to 773 km above 7 km. As apparent from Fig. 4, practically all wave energy is in the spectral region $L < 483$ km, corresponding to trigonometric variation with height in the lowest layer. This means that longer waves must predominantly be exponentially decreasing with height; exponentially increasing modes in the lowest layer must have vanishingly small amplitudes.

In the shear layer 2–7 km, the rays are no longer straight but curve upward in accordance with eq. (5.5), as noted by Klemp and Lilly (1980). According to ray tracing theory, L is constant along these curved rays, although H is not; this is because L_f depends on z, but not on x. Since most rays end up as almost vertical lines above the mountain, it is plausible that most of the wave energy is now channelled into this region. This is verified in Fig. 4 by the distribution of amplitudes in the calculated wave pattern.

Fig. 5 represents a case of negative wind shear in a layer from 4 to 10 km. In the bottom layer (0–4 km), L_f is constant, equal to 773 km, and all energy-transferring waves produced by the mountain will have horizontal wavelengths (L) smaller than this value. The rays in the bottom layer are straight sloping lines whose steepness (dz/dx) depends upon L according to (5.4) and (5.5). In the

upper layer above 10 km, on the other hand, $L_f =$ 483 km, and only rays with L smaller than 483 km can penetrate into this region. All rays with 483 km $< L <$ 773 km are therefore trapped within the shear layer where L_f decreases from 773 km at the base to 483 km at the top. Each of these rays will approach a horizontal asymptote at the level where $L_f = L$.

From these properties of the rays in the shear layer, we can draw conclusions about the wave pattern in this layer. With increasing downstream distance, the horizontal wavelength L in each isentropic surface tends towards the value of L_f in the same surface; in other words, the waves tend towards pure inertia waves, whose particle frequency equals f. Since the rays tend to become straight horizontal, parallel lines, $\nabla \cdot \mathbf{c}_g = 0$, and it follows from the wave action equation (5.7) that these waves are undamped in the downstream direction. Moreover, because in pure inertia waves the particles move in horizontal circles superimposed upon the mean flow, we must expect the horizontal streamlines to show undamped cycloid-shaped waves, whereas the vertical undulations of the θ-surfaces must tend to zero. The geostrophic streamlines must tend towards straight lines because there is no horizontal pressure gradient force connected with a pure inertia wave. Finally, it follows from (5.3) that the vertical wavelength $H \to 0$ when $L \to L_f$.

These conclusions are in agreement with the results obtained by Eliassen (1968) from analysis of the solution of the linear equations near the singularity $L = L_f$. He also pointed out, however, that the undamped wave train must be expected to break down due to shearing instability, because the vertical gradient of horizontal velocity will increase indefinitely downstream in the analytical solution.

Inspection of the calculated wave field in Fig. 5 shows that the local wavelength L in the shear layer does indeed approach L_f. The strong downstream damping in the shear layer of the vertical undulations of the θ-surfaces and the horizontal geostrophic streamlines are apparent, whereas the horizontal streamlines show cycloid-shaped waves without much damping. To study this behaviour, it would have been desirable to extend the calculation further downstream. This meets with the difficulty, however, that the vertical wavelength soon becomes too small to be resolved by the vertical grid.

In the last esxperiment, the result of which is shown in Fig. 6, there is a lower layer (0–4 km) with positive shear (10–16 m s^{-1}), a middle layer (4–10 km) with negative shear (16–10 m s^{-1}) and an upper layer with constant wind speed (10 m s^{-1}). Except in the lower layer, the wind structure is as in Fig. 5. But whereas in Fig. 5 rays with $L <$ 773 km are produced by the mountain and will enter the middle layer, in Fig. 6 only rays with $L <$ 483 km are produced by the mountain. These rays will enter the middle layer from below, but they will also leave this layer and escape into the top layer. Thus, no rays are trapped in the middle layer as in Fig. 5, and consequently, the wave energy is transferred upwards through the two shear layers in the near downstream region, and then spreads out in the upper layer. In a rough way, this explains the distribution of wavelengths and amplitudes of the computed wave field.

These examples show the important rôle played by the wind profile for the structure of meso-scale lee waves. The computation shown in Fig. 5 gives a confirmation of the results concerning the formation of inertia waves in shear layers obtained by Eliassen (1968). On the other hand, he was at the time not aware that this would be important only in layers of negative shear, not in layers of positive shear. This distinction was anticipated by Smith (1979), who argued that in the case of a positive shear layer, waves approaching a critical level from below must be evanescent and therefore reach the critical level with very small amplitude. The matter is complicated by the fact that waves with exponential z-dependence may also transfer energy upward, provided the upward-increasing and the upward-decreasing solutions are both present, which is quite conceivable in a limited layer. However, our integration experiments seem to support Smith's view that the exponential waves are nearly absent except close to the ground.

6. The turning of the streamlines

In all calculations, the final, nearly stationary flow has an anticyclonic turning between the upwind and downwind side. This turning is related to the mass transfer in the model. In the analytic model of Section 2, we obtain from the integrated

potential vorticity equation (2.15) and the mass continuity equation (2.5):

$$\frac{1}{f} v_x(x, \theta, t_1) = \frac{-p_\theta(x, \theta, t_1)}{-P_\theta} - 1$$

$$= -\frac{\partial}{\partial x} \int_0^{t_1} \frac{-p_\theta u}{-P_\theta} \, dt. \qquad (6.1)$$

Since the system does not permit infinite signal velocities, the air at $x = -\infty$ will remain in the undisturbed initial state at all times. Hence, v, $p - P$, and $u - U$ must vanish at $x = -\infty$, and (6.1) can be integrated to give

$$\frac{1}{f} v(x_1, \theta, t_1) = \int_{-\infty}^{x_1} \left[\frac{-p_\theta(x, \theta, t_1)}{-P_\theta} - 1 \right] dx$$

$$= -\int_0^{t_1} \left[\frac{(-p_\theta u)_{x=x_1}}{-P_\theta} - U \right] dt. \qquad (6.2)$$

This equation shows that $v(x_1, \theta, t_1)$ is proportional to the mass excess upstream of x_1 in a thin isentropic layer (or to the mass deficit downstream of x_1). In the last integral, the mass excess is expressed as the deficit of the mass flux through the plane $x = x_1$, integrated over time from the start.

Our result that v after a sufficiently long-time integration is positive at the inflow boundary and predominantly negative at the outflow boundary thus indicates a loss of air mass in the model, with an implied mass increase in the upstream and downstream environment. The loss of mass takes place during the transient stage of the integration (Fig. 7). The growth of the ground topography gives rise to two wave pulses which propagate away from the ridge in either direction, and which also cause a lasting mass displacement away from the ridge. Since the mass flux perturbation is seen to have the same direction at all levels, these wave pulses must be of the external type. Application of linear theory indicates that the system possesses only one external wave mode, with phase velocity $c \approx 313$ m s^{-1} relative to the fluid, and very weak dispersion; in the lower layers, this mode has close similarity to an acoustic wave and is the fastest wave possible in the system. Thus outside an interval extending from $(U - c)t$ to $(U + c)t$, no wave disturbances have yet arrived and the initial state prevails, with constant mass flux $(-P_\theta U)$ and $v = 0$. During the passage of the wave pulse, the mass flux is reduced on the upwind side and increased on the downwind side, and positive and negative values of v, respectively, develop on the two sides in accordance with (6.2), as shown schematically in Fig. 8. Finally, the motion settles to a steady state where the mass flux again assumes the initial constant value. However, since some of the mass has been pushed away by the ground topography during its growing stage, there is now a lasting mass deficit over the ridge and a corresponding anticyclonic bend. Fig. 8 shows schematically a streamline in horizontal projection, with the three flow regimes: initial, transient and stationary.

In our numerical calculations, the topographic ridge is centred at $x = 0$. At the inflow boundary ($x_A = -1750$ km), the first disturbance arrives after 1.5 h, and at the outflow boundary ($x_B = 2250$ km) a little later. This is in good agreement with the calculated speed of propagation of the external wave.

The effect of the mass loss in the system depends upon how the compensating mass gain in the environment has been distributed between the upstream and the downstream sides, or, in other words, to what extent the mass loss is caused by reduced inflow through the upstream boundary, or increased outflow through the downstream boundary. This depends again upon the properties of the conditions enforced at the open boundaries, or more specifically, how these boundary conditions function with respect to transmittance of the wave pulses that carry the excess mass away. We have performed integrations with different formulations of the inflow and outflow boundary conditons, but with everything else being the same. The results are identical with respect to the waves, but differ concerning the large-scale turning of the streamlines. The difference between two such stationary solutions at any θ-level consists very nearly of a constant velocity (Δv) in the y-direction and a corresponding constant gradient (Δm_x). This shows that the solutions differ simply by a different distribution between the upstream and downstream environment of the implied mass excess.

In the cases considered in this paper, the wind velocity is only about 4% of the external wave speed. One would therefore expect the upstream and downstream wave pulses set up by the growing mountain to be nearly symmetrical. With boundary conditions at the open boundaries allowing the

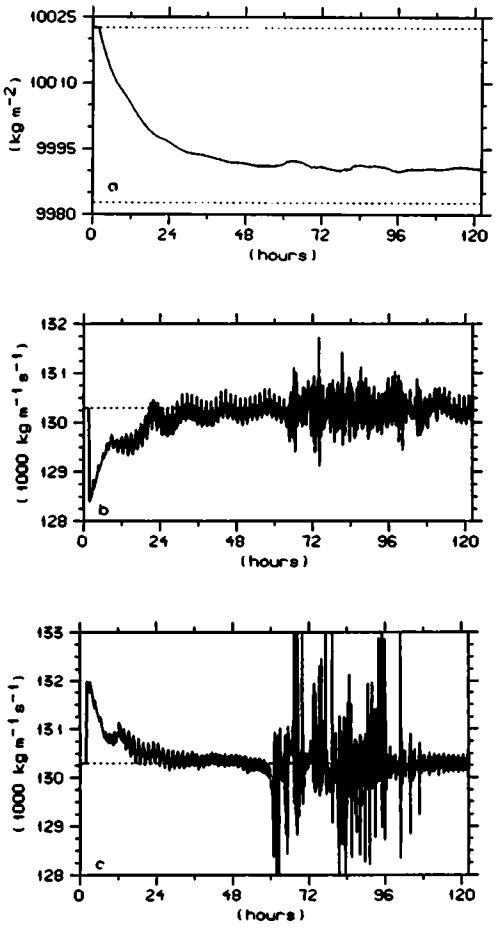

Fig. 7. (a) Total mass per unit area as function of time for Experiment 2. Upper dotted line: initial air mass. Lower dotted line: initial air mass minus the air mass displaced by the mountain. (b) Total mass flux through the inflow boundary and (c) through the outflow boundary as functions of time for Experiment 2.

waves to leave the system, nearly the same mass would be expected to leave by reduced inflow through x_A as by increased outflow through x_B. Consequently, we should expect $v_A \approx -v_B$ in the stationary stage. Apart from the fact that the outflow on the lee side is disturbed by meso-scale lee waves, this is seen to be quite well fulfilled in all our calculations. This we interpret as an indication that the Orlanski-type boundary conditions used in these calculations perform satisfactorily.

Fig. 7 shows the deviation of the vertically integrated mass flux from its initial value at the two open boundaries, and the total mass of the system, as functions of time for Experiment 2. The mass fluxes have been computed from (3.7) which is the consistent finite difference expression.

It will be seen from Fig. 7a that the mass loss is almost but not quite as large as the mass of air displaced by the mountain. This is an effect of the streamline turning: the positive v on the upwind side and the negative v on the lee side give Coriolis forces which push the air towards the mountain from both sides.

Our calculations indicate a slow decrease of the turning angle with increasing distance from the mountain on both sides. This corresponds to a gradual decrease of the mass flux carried by the external waves, and can be explained as a dispersive effect due to the earth's rotation.

7. The wave drag

Finally we consider the drag acting on the mountain. Per unit length of the mountain ridge, the force is

$$D = \int_{-\infty}^{+\infty} p(x, \theta_G) \frac{dz_G}{dx} dx. \tag{7.1}$$

The values obtained by numerical evaluation of this integral in Experiments 1–5 are listed in Table 1.

It appears that the values of D obtained from such integration experiments are quite sensitive to the outflow and inflow boundary conditions. The reason is that these conditions influence the *direction* of the current approaching the mountain, as explained in Section 6; and the direction in turn determines the geostrophic pressure gradient across the mountain ridge. Two solutions with somewhat different upstream wind directions will differ by a certain Δv, which is nearly constant in each isentropic surface. The corresponding difference $\Delta m_x = f\Delta v$ is also constant, and represents a difference in the cross-ridge pressure gradient and hence a difference ΔD in the drag. In a rough approximation we obtain

$$\Delta D = -f\Delta v\, \rho_G \int_{-\infty}^{+\infty} z_G dx \tag{7.2}$$

such that a positive Δv gives a reduced drag.

With this uncertainty in mind, we may compare the values of D obtained from the numerical

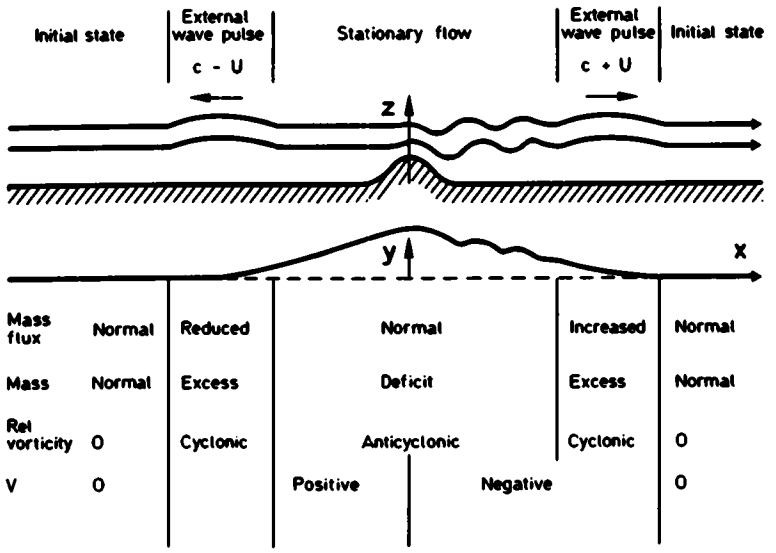

Fig. 8. Schematic diagram showing the effect of the mountain and the two external wave pulses on the isentropic heights, the horizontal streamlines, the mass flux, the mass distribution and the vorticity distribution.

calculations with theoretical values from linear theory. The force can be expressed as an integral over the Fourier spectrum by means of the Parseval formula. Smith (1979) has derived the explicit expression from linear theory for a barotropic basic current. He pointed out that only waves shorter than L_f contribute to the wave drag, and that the effect of rotation is to reduce the wave drag. With the mountain profile expressed as (2.10), Smith's formula may be written as

$$D = 4\pi\rho_G NUh^2 \int_{2af/U}^{\infty} \left[s^2 - \left(\frac{2af}{U} \right)^2 \right]^{1/2} |\hat{h}_1(s)|^2 ds, \tag{7.3}$$

where $\hat{h}_1(s)$ is the double-sided Fourier transform of the mountain profile function $h_1(\xi)$. Clearly, the integral decreases monotonically with increasing values of the inverse Rossby number $2af/U = 4\pi a/L_f$.

In our calculations, h_1 has the form (4.1) and

$$\hat{h}_1(s) = \frac{\pi}{2} \frac{\sin s}{s(\pi^2 - s^2)}. \tag{7.4}$$

For the barotropic case, $U = 13$ m s^{-1}, $2af/U = 2$, and a graphical evaluation of the integral in (7.3) gives the value 0.0313. This gives, with $h = 10$ m: $D = 8.6$ N m^{-1} as compared with 7.3 N m^{-1} obtained from our numerical integration experiment 1. With reference to eq. (7.2), the difference can be corrected by adding a velocity $\Delta v = -4 \times 10^{-3}$ m s^{-1} in the numerical solution for the 10 m mountain (corresponding to $\Delta v = -0.32$ m s^{-1} for the 800 m mountain).

From Experiment 2 we obtained $D = 1.61 \times 10^5$ N m^{-1}, whereas linear theory (7.3) gives only 0.55×10^5 N m^{-1}. We assume that this large difference is mainly a result of non-linearity.

In Experiments 3–5 with shear, D seems to increase with increasing surface wind, as one would expect, taking into account that the mountain height in Experiment 4 was reduced to 700 m.

8. Acknowledgements

This work has been partially supported by the Norwegian Research Council for Science and the Humanities (NAVF). The authors wish to thank Mr. Arne Bratseth, Prof. Ronald Smith, and Prof. Hans Økland for valuable discussions.

9. Appendix: List of symbols

a	half width of mountain ridge
A	suffix indicating inflow boundary

B	suffix indicating outflow boundary
c_g	group velocity
c_p	$= 1004\ \mathrm{m^2\ s^{-2}\ K^{-1}}$ specific heat capacity at constant pressure
D	wave drag
f	$= 1.3 \times 10^{-4}\ \mathrm{s^{-1}}$ Coriolis parameter
g	$= 9.8\ \mathrm{m\ s^{-2}}$ acceleration of gravity
G	suffix indicating lower boundary
h	height of mountain ridge (h_1 defined in Section 2)
H, L	horizontal, vertical wavelength
H_N, L_f	defined by equation (5.2)
j	numbering of θ-surfaces ($j = 0$ at the ground)
m	$= gz + \theta\Pi(p)$ Montgomery potential
M	initial equilibrium values of m
N	$= \left(\frac{g}{\theta}\frac{\partial\theta}{\partial z}\right)^{1/2} = 1.3 \times 10^{-2}\ \mathrm{s^{-1}}$ buoyancy frequency
p	pressure
P	initial equilibrium values of p
q	potential vorticity
R	$= 287\ \mathrm{m^2\ s^{-2}\ K^{-1}}$ specific gas constant
t	time
T	temperature. Suffix indicating upper boundary
u, v	Cartesian components of horizontal velocity
U	initial equilibrium values of u
x, y	horizontal Cartesian coordinates
z	height
$\delta_x, \delta_\theta, \delta_t$	centred finite differences
$\eta(x)$	$= y - y_0$ lateral trajectory displacement
$\eta_g(x)$	geostrophic trajectory displacement
ζ	vertical trajectory displacement
θ	$= c_pT/\Pi(p)$ potential temperature
κ	Rayleigh friction coefficient
$\Pi(p)$	$= c_p(p/1\ \mathrm{bar})^{R/c_p}$ Exner function
$\overline{(\ )}^x, \overline{(\ )}^\theta, \overline{(\ )}^y$	average over one grid mesh
ρ	density

REFERENCES

Charney, J. and Stern, M. E. 1962. On the stability of internal baroclinic jets in a rotating atmosphere. *J. Atmos. Sci. 19*, 159–172.

Eliassen, A. 1968. On mesoscale mountain waves on the rotating earth. *Geofys. Publ. 27–6*, 1–15.

Eliassen, A. and Rekustad, J. E. 1971. A numerical study of meso-scale mountain waves. *Geofys. Publ. 28–3*, 1–13.

Jones, W. L. 1967. Propagation of internal gravity waves in fluids with shear and rotation. *J. Fluid Mech. 30*, 439–448.

Klemp, J. B. and Lilly, D. K. 1978. Numerical simulation of hydrostatic mountain waves. *J. Atmos. Sci. 35*, 78–107.

Klemp, J. B. and Lilly, D. K. 1980. Mountain waves and momentum flux. *GARP. Publ. Series 23*, 115–141.

Orlanski, I. 1976. A simple boundary condition for unbounded hyperbolic flows. *J. Comput. Phys. 21*, 251–269.

Queney, P. 1947. Theory of perturbations in stratified currents with applications to airflow over mountain barriers. Misc. Report No. 23, Dept. of Met., Univ. of Chicago, 81 pp.

Queney, P. 1948. The problems of airflow over mountains: A summary of theoretical studies. *Bull. Amer. Meteorol. Soc. 29*, 16–26.

Shapiro, R. 1970. Smoothing, filtering, and boundary effects. *Rev. Geophys. Space Phys. 8*, 359–387.

Smith, R. B. 1979. The influence of the earth's rotation on mountain wave drag. *J. Atmos. Sci. 36*, 177–180.

Whitham, G. B. 1974. Dispersive waves and variational principles. In: *Nonlinear waves* (ed. Leibowich and Seebass). New York: Cornell University Press, pp. 139–169.